INTERNATIONAL JOURNAL OF INTEGRATED ENGINEERING
ISSN: 2229-838X e-ISSN: 2600-7916

IJIE

Vol. 17 No. 8 (2025) 313-323
https://publisher.uthm.edu.my/ojs/index.php/ijie

Flow Channelling and Restriction Zone Identification in Gas Mask Filter Cartridges using CFD

M. Hazimuddin Halif[1], Nor Azali Azmir[1]*

[1] *Department of Mechanical Engineering, Faculty of Mechanical Engineering and Manufacturing, Universiti Tun Hussein Onn Malaysia, Parit Raja, Batu Pahat, Johor, 86400, MALAYSIA*

*Corresponding Author: azali@uthm.edu.my
DOI: https://doi.org/10.30880/ijie.2025.17.08.026

Article Info

Received: 10 April 2025
Accepted: 3 August 2025
Available online: 31 December 2025

Keywords

Computational fluid dynamics, gas mask filter, flow channeling, pressure drop, air age, porous media, sorbent utilization

Abstract

Gas mask filters are critical for protecting against hazardous gases and airborne pollutants, yet their performance is strongly influenced by internal airflow behavior. In this study, Computational Fluid Dynamics (CFD) was employed to investigate pressure drop, velocity distribution, and air age (residence time) within a gas mask cartridge. The simulations revealed a maximum pressure drop of 41.94 Pa, well within acceptable breathing resistance limits, but with non-uniform distribution across the absorbent bed. Velocity contours showed flow channeling forming near the inlet and outlet, leaving regions further from the outlet underutilized. Air age analysis confirmed these patterns, with some regions achieving the required 0.67-0.80 s contact time for effective adsorption, while others fell below this threshold. These findings highlight that cartridge can affect airflow uniformity, adsorption efficiency, and sorbent utilization. The findings can guide the optimization of filter design in achieve more balanced flow distribution and improved performance.

1. Introduction

Workers in industries exposed to hazardous gases must be equipped with reliable respiratory protection to prevent inhalation of toxic contaminants. Gas mask filters play a critical role in safeguarding worker health, particularly in sectors such as oil and gas where airborne pollutants are common. In Malaysia, the National Institute of Occupational Safety and Health (NIOSH) highlights the importance of continuous monitoring and proper selection of respiratory protective equipment [1], [2]. Exposure to chemical and particulate pollutants has been linked to severe health risks, with global statistics estimating that a worker dies every 30 seconds due to toxic exposure and inadequate protective measures [3], [4]. These concerns underscore the need for certified and high-performance gas mask filters [5]-[7]. Although commercial gas mask filters are designed to capture harmful substances, their performance can degrade over time due to continuous use, high contaminant concentrations, and humid environmental conditions [8], [9].

Subsequently, the large surface area of filter media can lead to reduced adsorption efficiency [10], [11], while variations in cartridge geometry directly influence airflow resistance and sorbent utilization [12], [13]. Several studies have reported that airflow inside filters often becomes non-uniform, forming preferential flow paths where air follows the path of least resistance [14], [15]. This causes dead zones and recirculation regions, reducing filtration efficiency—particularly under elevated temperature and humidity, where density and flow behavior of air–vapor mixtures change significantly [16], [17]. Similar challenges have also been identified in chemical warfare canisters and CBRN respirator systems [18], [19]. Computational Fluid Dynamics (CFD) has proven to be a powerful tool for analyzing such flow behavior, allowing detailed visualization of internal airflow patterns, pressure losses, velocity fields, and dead-zone formation.

Previous research has demonstrated the effectiveness of CFD in assessing respirator performance and predicting transient flow behavior under various operating conditions [20]. Recent studies have integrated CFD with experimental validation and even virtual-reality-based design methods to further optimize cartridge performance [21], [22]. Beyond respirators, preferential flow modeling using CFD has been widely applied in porous media systems [23], adsorption studies, and activated carbon structures, emphasizing its usefulness in evaluating flow resistance, pressure drop, and filter service life [24]-[26]. Despite these advancements, limited studies have specifically examined how cartridge geometry influences internal flow distribution, particularly in terms of flow channeling, resistance zones, and residence time variations across the sorbent bed. This represents a significant knowledge gap in understanding how geometric design affects filter efficiency and sorbent utilization.

To address this gap, the present study employs CFD to investigate airflow behavior inside a gas mask filter cartridge. Three key parameters such pressure drop, velocity distribution, and air age (residence time) are analyzed to identify flow channeling, restricted zones, and underutilized regions within the filter medium. The results are presented through contour plots and plotted profiles to provide a clear interpretation of internal flow characteristics. This study aims to provide insights that support the optimization of gas mask filter geometry, ultimately improving airflow uniformity, adsorption efficacy, and overall respiratory protection performance under diverse environmental conditions [27].

2. Methodology

2.1 Geometry of Gas Mask Filter Cartridge

The filter cartridge used in this study was a 3M™ Organic Vapour Cartridge 6001 (A1) [28] and was developed using 3D scanner then import into SOLIDWORKS like (a) Casing of cartridge in Fig. 1, then imported into ANSYS Design Modeler for preprocessing. The internal airflow region was created using the "Fill" operation, which automatically detects enclosed cavities and generates a corresponding solid body representing the air domain shown at (b) Fluid domain of cartridge in Fig. 1.

To support the geometric representation used in the CFD model, the main dimensions of the gas mask cartridge are summarized from the scanned physical unit. The cartridge has an overall height of 107 mm, with a top length of 87 mm and a bottom length of 52 mm, which defines its tapered external profile. The outlet port measures 36 mm in diameter with an axial depth of 3.5 mm and functions as the single flow path. Internally, the filter assembly consists of a 2 mm paper pre-filter followed by a 10 mm activated charcoal layer, all enclosed within a 27 mm canister wall. The complete dimensional reference is provided in Appendix A.

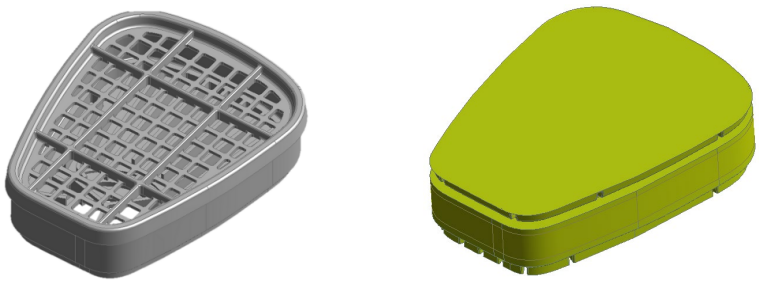

(a) **(b)**

Fig. 1 *The geometry of the gas mask cartridge (a) Casing; (b) Fluid domain*

2.2 Meshing of the Gas Mask Cartridge

As seen in Fig. 2, Meshing of the gas mask model and details at the inlet and outlet is shown. The total number of elements and nodes were present in Table 1 below:

Fig. 2 *Detail meshed model*

Int. Journal of Integrated Engineering Vol. 17 No. 8 (2025) p. 313-323

Table 1 *Number of nodes and elements for each geometry*

	Model		
Number of nodes	543,429	232,640	464,374
Number of elements	2,195,055	1,106,746	2,416,318

2.3 Governing Equation

Airflow inside the gas mask cartridge was modeled as an incompressible, steady-state flow governed by the continuity and Navier–Stokes momentum equations. The continuity equation is,

$$\nabla \cdot (\rho u) = 0 \tag{1}$$

where, ρ = fluid density (kg·m^{-3}), u = velocity vector (m·s^{-1}). Next, momentum equation is written as,

$$\rho(u \cdot \nabla)u = -\nabla p + \nabla \cdot (\mu \nabla u) + F \tag{2}$$

where, p = static pressure (Pa), μ = dynamic viscosity (kg·m^{-1}·s^{-1}), F = body force term (e.g., gravity), $(u \cdot \nabla)u$ = convective acceleration. Equations (1) and (2) form the basis for predicting velocity, pressure, and flow patterns inside the filter cartridge. To represent the filter layers, the Forchheimer porous media model was applied, as recommended by Park [18] and Rakyoung et al. [17]. This model extends Darcy's law by including inertial losses, making it more accurate for predicting flow resistance in fibrous and granular filter media. The governing relationship is expressed as:

$$-\frac{\Delta P}{L} = \alpha \mu V_s + \beta \rho V_s^2 \tag{3}$$

where ΔP is the pressure drop across a porous layer of thickness L, Vs is the superficial velocity, μ is the fluid viscosity, and α and β are the viscous and inertial resistance coefficients, respectively. In addition to airflow resistance, the concept of air age (residence time) was introduced as a performance indicator. Air age quantifies how long air remains within the filter media, reflecting the potential adsorption contact time. It is governed by:

$$\frac{\partial}{\partial x_i}(\rho u_i \tau) = \frac{\partial}{\partial x_i}\left(\frac{\mu_{eff}}{\sigma_\tau}\frac{\partial \tau}{\partial x_i}\right) + \rho \tag{4}$$

where, α = viscous resistance coefficient (m^{-2}), β = inertial resistance coefficient (m^{-1}). This formulation extends Darcy's law by including inertial losses, which is essential for porous media with moderate-to-high Reynolds numbers, such as granular activated carbon beds. The values of α and β used in this study were adopted from Su & Li (2009) [29] for commercial activated carbon cartridges with similar packing density and particle size (0.7–0.9 mm), ensuring consistency with experimentally validated porous-media data. Air age (residence time) was computed using a scalar transport equation implemented through a UDF. The governing equation is:

$$\nabla \cdot (\rho u \tau) = \nabla \cdot (\sigma \tau \mu eff \nabla \tau) + \rho \tag{5}$$

where τ = local air age (s), μ_eff = effective viscosity (turbulent + laminar), σ_τ = air-age turbulent Schmidt number. The source term ρ represents continuous inflow of fresh air, enabling the scalar field to increase with residence time inside the porous medium. This formulation is commonly used in CFD studies of adsorption filters because air age correlates directly with sorbent contact time and filtration efficiency.

2.4 Boundary Conditions and Parameter Assumptions

The canister inlet maintained a steady inhalation flow rate of 30 L/min throughout all simulations. Due to the fixed inlet area, the flow rate was converted to a mean velocity using the inlet area (A) of the canister opening, the mean inlet velocity (U) was calculated as which was then applied to the inlet boundary conditions. The gauge pressure of 0 Pa was imposed at the outlet, allowing the solver to determine the corresponding inlet pressure based on internal flow resistance. All solid walls were treated with a no-slip boundary condition. The SST k–ω turbulence model was selected because it provides accurate predictions in flows involving porous media, sharp pressure gradients, and near-wall behavior. This model has been widely used in respirator and filter-related CFD studies and is suitable for capturing transitional turbulence effects within the canister. Fig. 3 and Table 2 below show the boundary condition position and material properties that have been used:

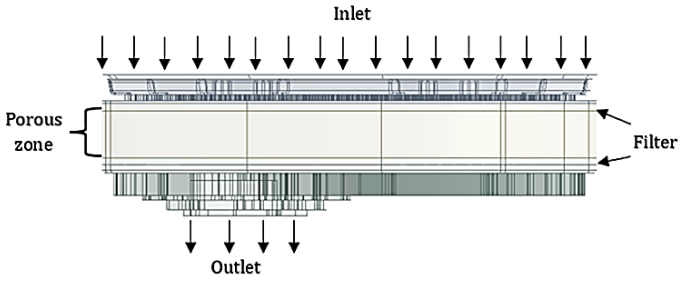

Fig. 3 *Boundary condition setup at the gas mask filter type 1*

Table 2 *Material properties*

Material	Air	Water vapor	Activated charcoal
Density (kg.m^{-3})	1.225	0.552	650
Specific heat (j.kg^{-1}. K^{-1})	1006.43	1000	800
Thermal conductivity (W.m^{-1}. K^{-1})	0.0242	2.5	0.27
Viscosity (kg.m^{-1}. s^{-1}) or porosity	0.000017894	0.483	0.5

2.5 Porous Media Parameters

The gas mask filter consisted of two porous media layers with pre-filter for coarse particle removal and an activated charcoal bed for gas adsorption. Both layers were modeled using the Darcy–Forchheimer equation. where μ is dynamic viscosity, α is permeability, is inertial coefficient, ρ is density, and v is superficial velocity. The assumed porous media parameters and physical properties are listed in Table 3. The coefficients listed were applied directly within ANSYS Fluent's Porous Zone settings, not through UDF coding. For each porous layer, the permeability α and inertial coefficient β were entered under Cell Zone Conditions at Porous Zone tab and listed in Porous Media Inputs, enabling Fluent to automatically apply the corresponding viscous and inertial momentum sinks. Only the air-age scalar uses UDF, all porous resistance effects rely on Fluents built-in model.

Table 3 *Material properties*

Layer	Porosity	Permeability (m^{-2}), α	Inertial coefficient (m^{-1}), β	Source
Pre-filter layer	0.90	1.52×10^{9}	6.41×10^{3}	Su and Li [29]
Activated charcoal bed	0.40	2.39×10^{9}	3.21×10^{4}	Su and Li [29]

2.5.1 Grid Independence Test

Grid Independence Test (GIT) was performed to ensure that the CFD results for the gas mask filter cartridge were not influenced by mesh density. Four mesh levels were generated by progressively refining the cells within the porous media and near-wall regions. The total element count ranged from approximately 1.1 million to 3.0 million, which is consistent with mesh resolutions commonly used in respirator CFD studies. For example, Rakyoung et al. [17] and Su and Li [13] employed meshes between 1-4 million elements to achieve stable predictions of pressure drop and flow distribution through porous filter layers. The velocity across the cartridge was monitored as the refinement criterion. As shown in Fig. 4 and summarized in Table 4.

Int. Journal of Integrated Engineering Vol. 17 No. 8 (2025) p. 313-323

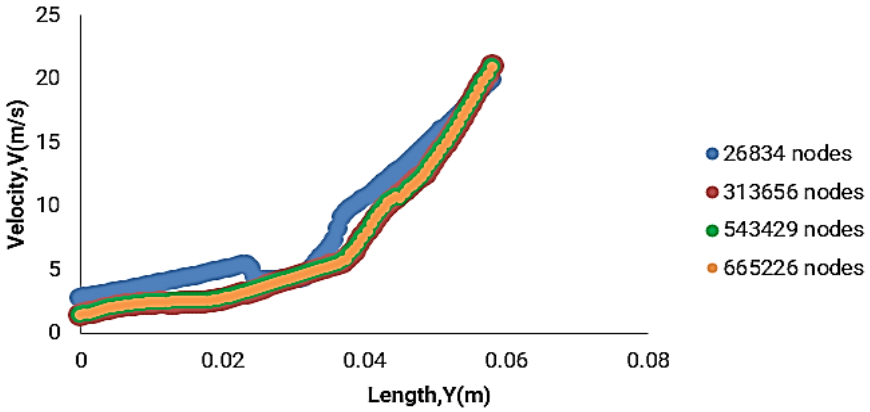

Fig. 4 *GIT chart for geometry*

Table 4 *Elements and nodes for each geometry*

Parameters	Type 1	Type 2	Type 3
Number of elements	2,195,055	1,106,746	2,416,318
Number of nodes	543,429	232,640	464,374

3. Results

This section presents the results of the computational analysis performed to evaluate the flow parameters within the gas mask filter cartridge

3.1 Pressure Drops

Pressure contours were taken to visualize the resistance encountered by airflow as it passed through the pre-filter and activated charcoal layers. Fig. 5 shows the pressure field using a cross-sectional cut through the centre of the canister. The contour observed gradual in pressure reduction from the inlet region toward the outlet, as expected for porous media region. The highest pressure occurs immediately downstream of the inlet, where flow first encounters the pre-filter, while the lowest pressure appears at the outlet where a zero-gauge boundary condition is imposed. The activated charcoal zone exhibits a visibly larger pressure gradient than the pre-filter, consistent with its lower permeability.

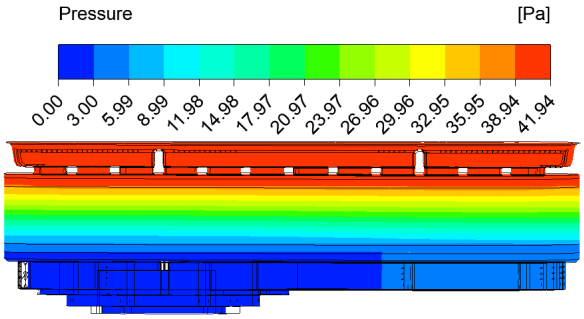

Fig. 5 *Pressure drop within filter*

A top-view contour of the charcoal bed in Fig. 6 reveals non-uniform pressure distribution across the absorbent surface. Regions located farther from the outlet exhibit higher local pressure, indicating increased flow resistance and reduced air penetration. Conversely, areas adjacent to the outlet show lower pressure, suggesting these regions function as preferential pathways for airflow. The color scale clearly highlights these differences, supporting the identification of high-resistance and low-resistance regions across the bed.To quantify the gradient, a reference line was drawn across the charcoal surface, and the pressure values were sampled along this line in Fig. 6 The resulting plot confirms a monotonically decreasing trend from the outer region toward the outlet, with a pressure difference of approximately 7-10 Pa across the surface. This reinforces the contour interpretation and confirms that the uneven pressure field is geometry-dependent.

These findings are in agreement with Rakyoung et al. [17], who demonstrated that outlet positioning and cartridge geometry significantly influence internal pressure gradients and contribute to the development of flow channeling zones. The observed pressure gradient across the bed in this study further highlights outlet placement in determining the overall flow distribution. To illustrate this effect, a pressure gradient was plotted along a reference line, as shown in Fig. 7, which confirms the gradual increase in resistance with flow distance.

The pressure drop increase as the distance travel along the surface reflecting towards previous contour shown. The increase in pressure drop with travel distance reflects the presence of high-resistance regions, which potentially restrict airflow and lead to uneven sorbent utilization. Similarly, Park [18] reported that pressure loss in activated carbon canisters increases with path length and medium thickness, supporting the higher resistance measured in distant regions of the bed. The combination of top-view contours and gradient plots demonstrates that some regions within the bed become more difficult for airflow to penetrate, thereby reinforcing the presence of preferential flow channels.

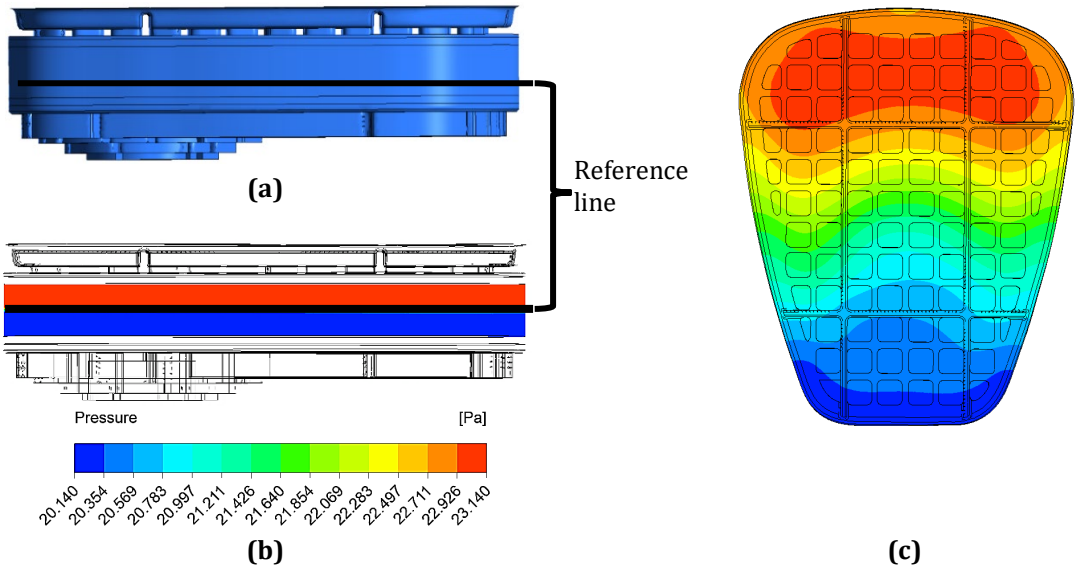

Fig. 6 *(a) Side view cartridge; (b) Cross-sectional view with reference line; (c) Top view contour of the activated charcoal bed*

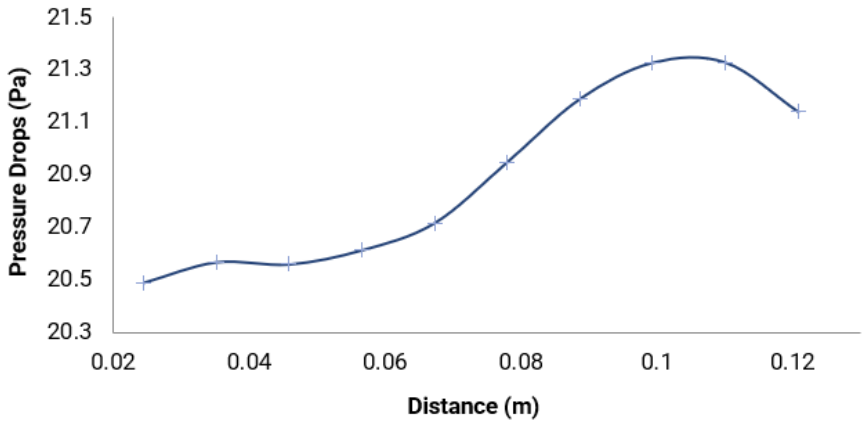

Fig. 7 *Pressure drop along reference line*

3.2 Velocity Distribution

Velocity contours were examined to assess how airflow propagates through the pre-filter and activated charcoal layers. All velocity plots were presented with a consistent color map and units (m/s), including clear legends and figure numbering for ease of comparison. Fig. 7(a) shows the velocity magnitude on a mid-plane cross-section. The airflow accelerates as it enters the pre-filter due to geometric contraction and then decelerates upon encountering the more resistive charcoal bed. The highest velocities occur along pathways closest to the outlet, where the flow experiences lower hydraulic resistance. In contrast, areas that are farther from the outlet show significantly lower velocities, reflecting increased porous drag and longer flow paths.

Int. Journal of Integrated Engineering Vol. 17 No. 8 (2025) p. 313-323

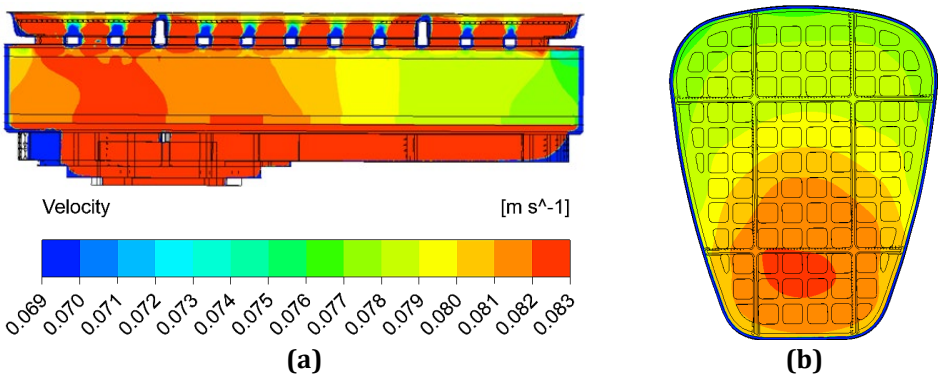

Fig. 7 *Velocity contour (a) Side view; (b) Top view at absorbent surface*

A top-view velocity contour of the charcoal surface in Fig. 7(b) reveals clear non-uniformity in flow distribution. Regions adjacent to the outlet demonstrate velocities of approximately 0.18-0.22 m/s, while peripheral zones exhibit much lower values, ranging from 0.05-0.09 m/s. This represents a velocity variation of nearly 60-70% across the absorbent surface, indicating the presence of flow channels. Such non-uniformity is consistent with results reported by Rakyoung et al. [17], who showed that the location of the outlet significantly biases internal flow paths within the filter. To visible and quantify this behavior, a velocity profile was extracted along a reference line drawn across the top surface of the charcoal bed Fig. 8. The profile shows a clear downward trend as the distance from the outlet increases, confirming that airflow travels through the low-resistance central region while bypassing outer sections of the absorbent bed. This uneven flow distribution is directly associated with geometry-dependent resistance differences across the bed and may reduce local sorbent utilization. These results collectively indicate that cartridge geometry—particularly outlet placement and surface layout—plays a major role in shaping velocity distributions within the porous medium.

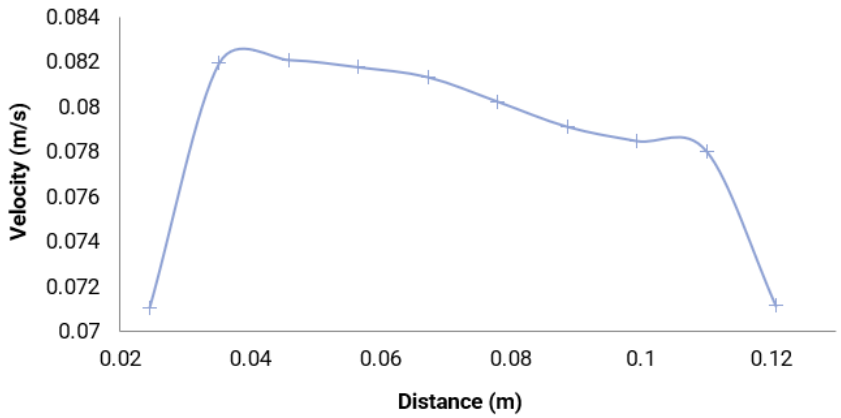

Fig. 8 *Velocity profile along refference line*

3.3 Air Age Distribution

The air-age scalar was computed using a dedicated UDF to evaluate the residence time of air within the porous media. Air age serves as a key indicator of adsorption potential, as longer residence times correspond to improved contact between the air stream and the sorbent. The contours and plots are presented with units in seconds and labeled color scales for interpretation. Fig. 9 illustrates the air-age distribution along a vertical cross-section. The air-age field is strongly influenced by flow channeling: regions near the inlet and outlet exhibit shorter residence times due to higher velocities, while the central and upper portions of the charcoal bed display higher air-age values, indicating zones of slower flow renewal.

Fig. 10 further highlights this pattern. The air age near the preferred flow channel (adjacent to the outlet) ranges from 0.30-0.45 s, whereas regions located farther away reach 0.60-0.75 s, and in some localized areas exceed 0.80s. According to Su and Li [29], an effective residence time of approximately 0.67-0.80 s is required for meaningful gas–sorbent interaction in activated charcoal. The present results show that only portions of the bed achieve this threshold, while other regions fall below it.

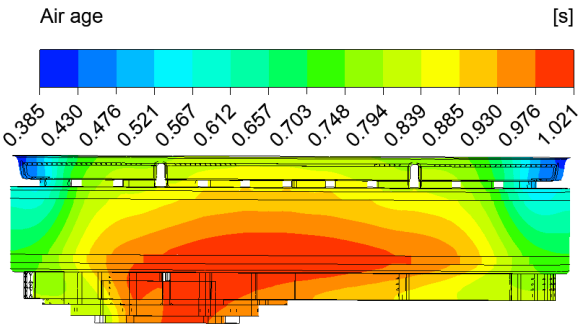

Fig. 9 *Air age distribution side view*

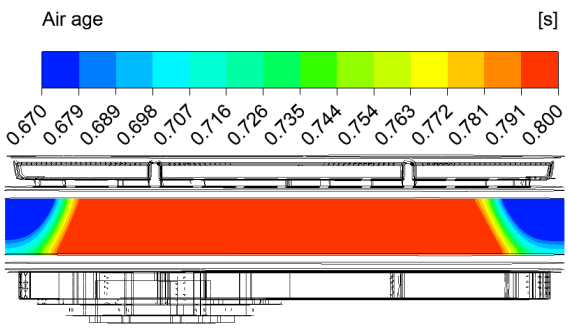

Fig. 10 *Air age at absorbent*

To quantify this behavior, an air-age profile was extracted along a reference line across the absorbent surface Fig. 11. The plot shows a distinct peak in air residence time at mid-span distances, confirming that air tends to accumulate longer in the central region of the charcoal layer, where local flow velocities are the lowest. Conversely, areas near the outlet show rapid air turnover, resulting in lower residence times. Similar preferential flow behavior has been reported in porous bed studies [25], [29], demonstrating that airflow tends to concentrate in regions of lowest resistance, leaving adjacent areas underutilized. These results indicate that although some regions of the bed meet the required residence-time criterion for efficient adsorption, a significant fraction of the charcoal volume is underutilized due to non-uniform flow distribution. This suggests that modifications to the outlet positioning or internal flow-guiding structures may be necessary to achieve more uniform air residence and improve overall sorbent efficiency.

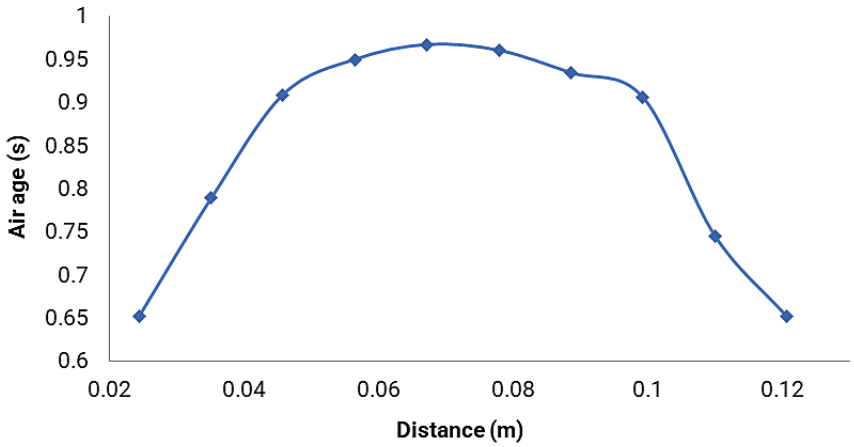

Fig. 11 *Air age at absorbent*

3.4 Comparison with Literature Value

A validation of the predicted internal flow behaviour was performed by comparing the present CFD results with benchmark studies on gas mask cartridges with similar geometries and porous media configurations. Two well-established references like Luxmoore and Ferrand [25], who analysed an improved respirator cartridge using experiments and CFD, and Su and Li [29], who performed a detailed aerodynamic study of a commercial gas mask canister containing an activated carbon layer. Both works employed a volumetric flow rate of 30 L/min and reported velocity fields inside the porous adsorption bed, enabling direct comparison with the present simulation.

Luxmoore and Ferrand [25] reported that internal velocity magnitudes within the porous bed ranged from 0.05–0.25 m/s, with localized high-velocity streaks near inlet perforations reaching 0.28–0.32 m/s. Low-velocity regions were observed along the peripheral annulus and inner wall surfaces. Their velocity distribution patterns including preferential jetting through the main inlet holes and gradual reduction toward the outer radius are consistent with the flow structures observed in the present cartridge geometry. Similarly, Su and Li [29] demonstrated that the activated carbon layer in a commercial canister exhibits low-velocity regions of 0.02–0.06 m/s and high-velocity zones up to 0.18-0.26 m/s at the same flow rate of 30 L/min. Their tangential velocity position profiles confirm that porous flow generates a strong velocity gradient between the central jet region and the outer stagnant pockets, a characteristic also reproduced in the current study.

The present simulation predicts velocity magnitudes of 0.05–0.09 m/s in peripheral regions and 0.18–0.22 m/s near the outlet zone. These values lie well within the ranges reported by Luxmoore and Ferrand [25] and Su

and Li [29]. Furthermore, the spatial flow patterns specifically, the presence of a peripheral low-velocity ring, local acceleration through inlet perforations, and re-acceleration near the outlet show close qualitative correspondence with the experimentally validated studies. Overall, the agreement in both velocity magnitude and flow structure indicates that the current CFD model demonstrates physically realistic internal flow behaviour and is consistent with validated gas mask cartridge simulations in the literature. Therefore, the present model can be considered reliable for predicting internal flow distribution, pressure drop, and air-age characteristics within the cartridge.

4. Conclusions

This study used Computational Fluid Dynamics (CFD) to analyze airflow behavior within a gas mask filter cartridge, focusing on pressure drop, velocity distribution, and air age as key performance indicators. The simulation results show that pressure resistance increases progressively with distance from the outlet, with a maximum pressure drop of 41.94 Pa—well within acceptable inhalation resistance limits. However, this pressure distribution was non-uniform, and regions located farther from the outlet experienced noticeably higher resistance. Velocity contours revealed the formation of preferential flow channels, where air primarily traveled through low-resistance pathways near the inlet and outlet, while other regions—particularly the upper and peripheral zones of the absorbent bed—experienced significantly lower velocities. This uneven flow behavior directly contributed to non-uniform residence times within the sorbent layer. Air-age analysis showed that certain zones achieved the required 0.67-0.80 s contact time for efficient adsorption, whereas other zones fell below this threshold, indicating underutilization of the activated carbon. The combined findings confirm that cartridge geometry, especially outlet positioning, strongly influences internal flow uniformity and sorbent utilization. Flow channeling and high-resistance zones reduce the effective working volume of the absorbent material, potentially shortening service life and limiting overall filtration performance.

To enhance gas mask filter efficiency, future cartridge designs should prioritize geometrical optimization to achieve more uniform flow distribution across the porous media. Strategies may include repositioning the outlet, adjusting internal flow paths, or modifying porous media resistance to minimize stagnant regions and improve overall sorbent utilization. Further work should include experimental validation, mesh-independence refinement, and parametric studies covering varying flow rates, humidity levels, and sorbent packing configurations to strengthen the reliability and applicability of the findings

Acknowledgement

This research was supported by Universiti Tun Hussein Onn Malaysia (UTHM) through Tier 1 (vot Q901).

Conflict of Interest

The authors declare that there is no conflict of interest regarding the publication of the paper.

Author Contribution

The authors are responsible for the study conception, research design, data collection, data analysis, result interpretation and manuscript drafting.

Appendix A: Geometry Dimensions

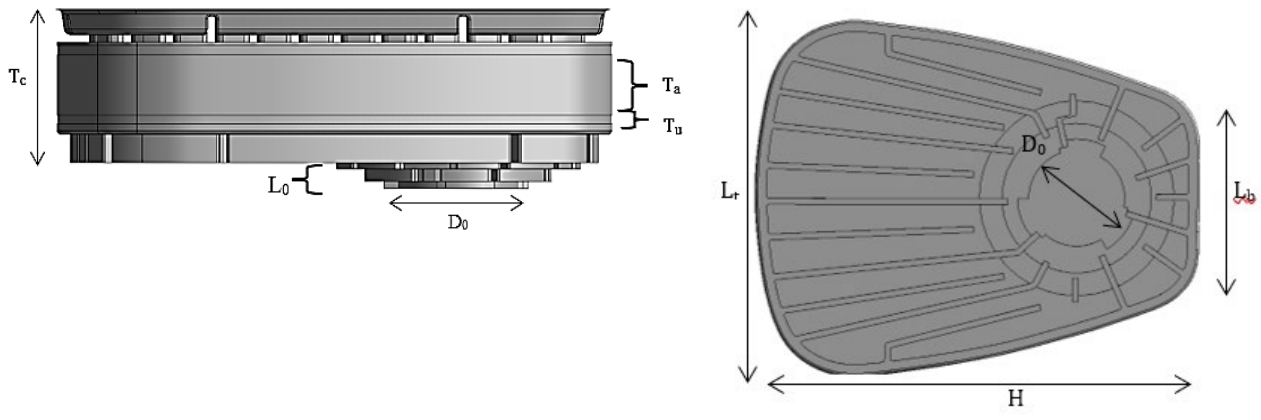

Fig. A1 *The geometric dimensions (a) Side view; (b) Lower view*

Table A1 *Dimension of cartridge*

Parameters	Type 1
Outlet diameter, D_o	36 mm
Outlet length, L_o	3.5 mm
Activated charcoal thickness, T_a	10 mm
Paper filter thickness, T_u	2 mm
Canister thickness, T_c	27 mm
Canister height, H	107 mm
Bottom length, L_b	52 mm
Top length, L_t	87 mm

References

[1] NIOSH (1996). NIOSH guide to the selection and use of particulate respirators certified under 42 CFR part 84. U.S. Department of Health and Human Services, Public Health Service, Centers for Disease Control, National Institute for Occupational Safety and Health. DHHS (NIOSH) Publication No. 96-101.

[2] Roxana Z. Witter, Liliana Tenney, Suzanne Clark & Lee S. Newman (2014) Occupational exposures in the oil and gas extraction industry: State of the science and research recommendations, *American Journal of Industrial Medicine*, *57(7)*, 847-856, https://doi.org/10.1002/ajim.22316

[3] Roman Ligotski, Uta Sager, Ute Schneiderwind, Christof Asbach & Frank Schmidt (2019) Prediction of VOC adsorption performance for estimation of service life of activated carbon based filter media for indoor air purification, *Building and Environment*, *149*, 146-156, https://doi.org/10.1016/j.buildenv.2018.12.001

[4] ISHN (2019, 15 March). A worker dies of toxic exposure in the workplace every 30 seconds. https://www.ishn.com/articles/110415-a-worker-dies-of-toxic-exposure-in-the-workplace-every-30-seconds

[5] Agnieszka Brochocka & Krzysztof Makowski (2020) General guidelines for the selection and use of filtering respiratory protective devices, In *Nanoaerosols, Air Filtering and Respiratory Protection* (pp. 199-213). CRC Press. https://doi.org/10.1201/9781003050070-8

[6] Norbert Riefler, Martina Ulrich, Marko Morshäuser & Udo Fritsching (2018) Particle penetration in fiber filters, *Particuology*, *40*, 70-79, https://doi.org/10.1016/j.partic.2017.11.008

[7] K. S. Kim (2004) Occupational health: Respiratory protection in the industry, *Jurutera*, *2004(9)*, 46-52.

[8] Paul Schulte, Charles Geraci, Ralph Zumwalde, Mark Hoover & Eileen Kuempel (2008) Occupational risk management of engineered nanoparticles. *Journal of Occupational and Environmental Hygiene*, *5(4)*, 239-249, https://doi.org/10.1080/15459620801907840

[9] Eric J. Esswein, John Snawder, Bradley King, Michael Breitenstein, Marissa Alexander-Scott & Max Kiefer (2014) Evaluation of some potential chemical exposure risks during flowback operations in unconventional oil and gas extraction: preliminary results. *Journal of Occupational and Environmental Hygiene*, *11(10)*, D174-D184.

[10] Yat Huang Yau, B. T. Chew & A. Z. A. Saifullah (2012) Thermal comfort temperature range study for workers in a factory in Malaysia. *American Journal of Engineering Research*, *2*, 1218-1223.

[11] 3M Australia Pty Ltd. Occupational health & environmental safety division. https://multimedia.3m.com/mws/media/447121O/filter-change-out-brochure.pdf

[12] N. M. R. Noraini, Nor Azali Azmir, Ishkrizat Taib, Amir Abdullah Muhamad Damanhuri, Mohd Idain Fahmy Rosley & Azil Bahari Alias (2022) Analysis of preferential flow at the front mesh cartridge of the gas mask filter: Cases in Malaysia climate environment, *Journal of Advanced Research in Applied Sciences and Engineering Technology*, *28(3)*, 299-311, https://doi.org/10.37934/araset.28.3.299311

[13] Su, Yin-Chia & Chun-Chi Li (2015) Computational fluid dynamics simulations and tests for improving industrial-grade gas mask canisters, *Advances in Mechanical Engineering*, *7(8)*, 1687814015596297, https://doi.org/10.1177/1687814015596297

[14] Ozen, M. (2014). Ansys: Meshing workshop. *Ozen Engineering, INC*.

[15] Sidra Shaoor Kiani, Amjad Farooq, Masroor Ahmad, Naseem Irfan, Mohsan Nawaz & Muhammad Asim Irshad (2021) Impregnation on activated carbon for removal of chemical warfare agents (CWAs) and radioactive content, *Environmental Science and Pollution Research*, *28(43)*, 60477-60494, https://doi.org/10.1007/s11356-021-15973-1

[16] A. Mohammad-Khah & R. Ansari (2009) Activated charcoal: Preparation, characterization and applications, *International Journal of Chemical Technology Research*, *1(4)*, 859-864.

[17] Rakyoung Jeon, Kihyun Kwon, Soonmin Yoon, Myungkyu Park, Changha Lee & Min Oh (2019) Analysis of a gas mask using CFD simulation, *Korean Chemical Engineering Research*, *57(4)*, 475-483, https://doi.org/10.9713/kcer.2019.57.4.475

[18] Park Yong-Hwan, (2017) Pressure loss in canisters with conditions of activated carbon particles, *Fire Science and Engineering*, *31*(4), 7-11, https://doi.org/10.7731/KIFSE.2017.31.4.007

[19] Samuel GA Wood, Nilanjan Chakraborty, Martin W. Smith & Mark J. Summers (2019), A computational fluid dynamics analysis of transient flow through a generic chemical biological radiological and nuclear respirator canister, *Chemical Engineering Research and Design*, *142*, 13-24, https://doi.org/10.1016/j.cherd.2018.12.006

[20] Fangfang Si, Pengfei Lian, Derui Yang, Guolin Han, Shaoyue Hao, and Pingwei Ye (2019) 3D numerical simulation of aerodynamic characteristics of a gas filter, *Journal of Applied Mathematics and Physics*, *7(8)*, 1920-1928, https://doi.org/10.4236/jamp.2019.78132

[21] Gustavo Aparicio-Mauricio, Francisca A. Rodríguez, Joep JH Pijpers, Martín R. Cruz-Díaz & Eligio P. Rivero, (2020) CFD modeling of residence time distribution and experimental validation in a redox flow battery using free and porous flow, *Journal of Energy Storage*, *29*, 101337, https://doi.org/10.1016/j.electacta.2019.135319

[22] Phuong Thi Minh Tran, Jie Rui Ngoh & Rajasekhar Balasubramanian (2020) Assessment of the integrated personal exposure to particulate emissions in urban micro-environments: A pilot study, *Aerosol and Air Quality Research*, *20(2)*, 341-357, https://doi.org/10.4209/aaqr.2019.04.0201

[23] I. A. Magomedov & Z. S. Sebaeva (2020, April), Comparative study of finite element analysis software packages, In *Journal of Physics: Conference Series* (Vol. 1515, No. 3, p. 032073), IOP Publishing. https://doi.org/10.1088/1742-6596/1515/3/032073

[24] Rakyoung Jeon, Shin Hyuk Kim, Kwangjun Ko, Kihyun Kwon, Myungkyu Park, Ireh Seo, Min Oh & Chang-Ha Lee (2023) Advanced cartridge design for a gas respiratory protection system using experiments, CFD simulation and virtual reality, *Journal of Cleaner Production*, *426*, 139101, https://doi.org/10.1016/j.jclepro.2023.136408

[25] R. J. Luxmoore & L. A. Ferrand (1993) Towards pore-scale analysis of preferential flow and chemical transport In *Water Flow and Solute Transport in Soils: Developments and Applications in Memoriam Eshel Bresler (1930–1991)* (pp. 45-60). Berlin, Heidelberg: Springer Berlin Heidelberg, https://doi.org/10.1007/978-3-642-77947-3

[26] Peng Huo, Yang Zhang, Lijia Zhang, Mei Yang, Wenjie Wei, Xin Zhang, Jianxiao Yang & Yuanxun Zhang (2021) Insight into the adsorption process of ethanol and water on the pore structure and surface chemistry properties engineered activated carbon fibers, *Industrial & Engineering Chemistry Research*, *60(30)*, 11141-11150, https://doi.org/10.1021/acs.iecr.1c02005

[27] Dan Zhao, Praveen K. Thallapally, Camille Petit & Jorge Gascon (2019), Advanced porous materials: design, synthesis, and applications in sustainability, *ACS Sustainable Chemistry & Engineering*, *7(9)*, 7997-7998, https://doi.org/10.1021/acssuschemeng.9b02021

[28] 3M, 2025. *3M™ Organic Vapour Cartridge 6001 (A1).* 3M Personal Safety: https://www.3m.com/3M/en_US/p/d/b00013849/

[29] Y.-C. Su, & C.-C. Li (2009) Study on airflow uniformity and residence time in gas mask canisters, *Journal of Hazardous Materials*, *168(2-3)*, 1470-1477.